



Cite this: DOI: 10.1039/d5ee02650d

## Tailored self-assembled monolayer molecules for perovskite/PERC tandem solar cells with efficiencies over 30%

So Jeong Park,<sup>a</sup> Changhoon Yu,<sup>†a</sup> Kyu In Shim,<sup>b</sup> Geon Pyo Hong,<sup>ib</sup><sup>a</sup>  
Sunwu Song,<sup>a</sup> Jae Hyun Park,<sup>ab</sup> Sun Kyung Hwang,<sup>a</sup> Yeo Jin Choi,<sup>a</sup>  
Jeong Woo Han,<sup>ib</sup><sup>ab</sup> Min Sang Kwon,<sup>ib</sup><sup>\*ab</sup> Ik Jae Park<sup>\*cd</sup> and  
Jin Young Kim<sup>ib</sup><sup>\*abe</sup>

The commercialization of perovskite/Si tandem solar cells requires low product costs, achievable through high efficiency and inexpensive components. Here, we report a highly efficient monolithic perovskite tandem device utilizing a commercial passivated emitter and rear cell (PERC), with the aid of a fluorine-substituted carbazole-based self-assembled monolayer (SAM). Modified SAM molecules enhanced charge transfer due to the larger dipole moments resulting from asymmetric charge distribution. The negative adsorption energy and well-ordered molecules alleviated residual stress in perovskite films and reduced trap density at the interfaces, leading to suppressed non-radiative recombination and improved open-circuit voltage of the perovskite top cell. As a result, the best single-junction perovskite cell exhibits a certified efficiency of 20.14%, with a good operational stability maintaining 90% of its initial efficiency after 1500 hours. The best perovskite/Si tandem cell, fabricated with cost-effective PERC bottom cells, exhibits a conversion efficiency of 30.05%, which is the highest among PERC-based perovskite tandem solar cells.

Received 13th May 2025,  
Accepted 6th August 2025

DOI: 10.1039/d5ee02650d

rsc.li/ees

### Broader context

To overcome the hurdles in commercializing perovskite/Si tandem solar cells, it is crucial to decrease power production costs by achieving high efficiency with cost-effective materials. In this study, we demonstrate a perovskite/Si tandem solar cell with an efficiency over 30% with a fluorine-substituted carbazole-based self-assembled monolayer (SAM) using a commercial passivated emitter and rear cell (PERC) composed of scalable and low-cost components. The fluorine substitution strategy induces an asymmetric molecular structure, resulting in a larger dipole moment. It increases the work function and deepens the highest molecular orbital (HOMO) level, thereby improving energy level alignment at the perovskite/SAM interfaces and facilitating effective charge transfer. Additionally, modified SAM molecules lead to energetically favorable adsorption, stabilize the perovskite lattice, and prevent the formation of  $I^-$  vacancies, resulting in improved operational stability of wide-bandgap perovskite solar cells by inhibiting halide segregation. We achieved a power conversion efficiency (PCE) of 21.62% in a single-junction wide-bandgap perovskite top cell that retained 90% of its initial efficiency after 1500 hours of continuous illumination. Furthermore, we achieved a PCE of 30.05% in a monolithic 2T perovskite/PERC tandem cell, surpassing the previous highest efficiency for PERC-based tandem solar cells.

### Introduction

Tandem solar cells employing halide perovskites are attracting significant attention as a high-efficiency photoenergy conversion device.<sup>1–8</sup> For example, the efficiency of the monolithic 2-terminal (2T) perovskite/Si tandem cells has rapidly increased to 34.6%, surpassing the theoretical Shockley–Queisser (S–Q) limit by reducing non-absorption and thermalization losses.<sup>9–15</sup> Perovskite materials are promising candidates for the top cell of Si tandem devices, due to their high absorption coefficient, tunable bandgap, and ease of processing through various

<sup>a</sup> Department of Materials Science and Engineering, Seoul National University, Seoul 08826, Republic of Korea. E-mail: minsang@snu.ac.kr, jykim.mse@snu.ac.kr

<sup>b</sup> Research Institute of Advanced Materials (RIAM), Seoul National University, Seoul 08826, Republic of Korea

<sup>c</sup> Department of Materials Physics, Sookmyung Women's University, Seoul 04310, Republic of Korea. E-mail: parkij@sookmyung.ac.kr

<sup>d</sup> Institute of Advanced Materials and Systems, Sookmyung Women's University, Seoul 04310, Republic of Korea

<sup>e</sup> School of Transdisciplinary Innovations, Seoul National University, Seoul 08826, Republic of Korea

<sup>†</sup> These authors contributed equally to this work.

deposition methods.<sup>16–21</sup> To fully utilize the advantages of high-efficiency perovskite/Si tandem cells, it is crucial to reduce fabrication and materials costs, ensuring that their power generation cost becomes low enough to enable commercialization. In this context, the use of widely used silicon bottom cells, such as the passivated emitter and rear cell (PERC) and the tunnel oxide passivated contact (TOPCon) cell, is desirable.<sup>22–24</sup>

Since Albrecht *et al.* introduced carbazole-based self-assembled monolayers (SAMs) with phosphonic acid anchoring groups as hole extraction layers for the p–i–n type inverted structures, these materials have been most widely used in highly efficient perovskite-based tandem solar cells.<sup>2,25–30</sup> SAMs exhibit high surface coverage on substrates, forming conformal layers regardless of morphology when applied *via* a solution process, even on micro-sized textured silicon. In addition, the ultra-thin thickness and large bandgap of SAMs effectively mitigate parasitic absorption losses, while their favourable energy band levels facilitate efficient hole extraction.<sup>2</sup> Representative SAMs used in perovskite solar cells include 2PACz ([2-(9H-carbazol-9-yl)ethyl]phosphonic acid) and its derivatives, such as MeO-2PACz and Me-4PACz. These derivatives are modified by altering the length of methyl groups or making substitutions in the carbazole moiety to tune their properties.<sup>25</sup> Substituted functional groups, such as methoxy or methyl groups, interact with perovskite films and effectively passivate defects at the interfaces.<sup>31,32</sup> However, these substitutions also influence the molecular symmetry and the local charge distribution, thereby affecting the dipole moment and energy

band levels.<sup>33,34</sup> Therefore, designing SAM molecules is crucial for achieving highly efficient photovoltaics.

In this work, we present a strategy to develop a highly efficient and cost-effective 2T perovskite/Si tandem cell incorporating a commercial PERC cell. The strategy involves the substitution of one methoxy group of [4-(3,6-dimethoxy-9H-carbazol-9-yl)butyl]phosphonic acid (MeO-4PACz) with fluorine, resulting in a large dipole moment due to the asymmetric molecular structure (F-MeO-4PACz). The modification led to an increased work function (WF), a deeper highest occupied molecular orbital (HOMO) level, and improved alignment of the SAM molecules. These altered properties of the F-MeO-4PACz molecules suppressed charge recombination and enhanced charge transfer at the perovskite/SAM interface. Consequently, the perovskite single-junction device with the fluorine-substituted SAM exhibited improved photovoltage and a high certified efficiency of 20.14%, which retained 90% of its initial efficiency after continuous operation for 1500 hours. Furthermore, the highest-performing 2T perovskite/Si tandem cell, with a power conversion efficiency (PCE) of 30.05%, was successfully fabricated using a commercial PERC.

## Results and discussion

### Designing SAM molecules

Fig. 1a depicts the molecular structures and the electrostatic potential (ESP) distributions of a series of SAM molecules with varying substituents and aliphatic chain lengths ( $n = 2, 4$ ),

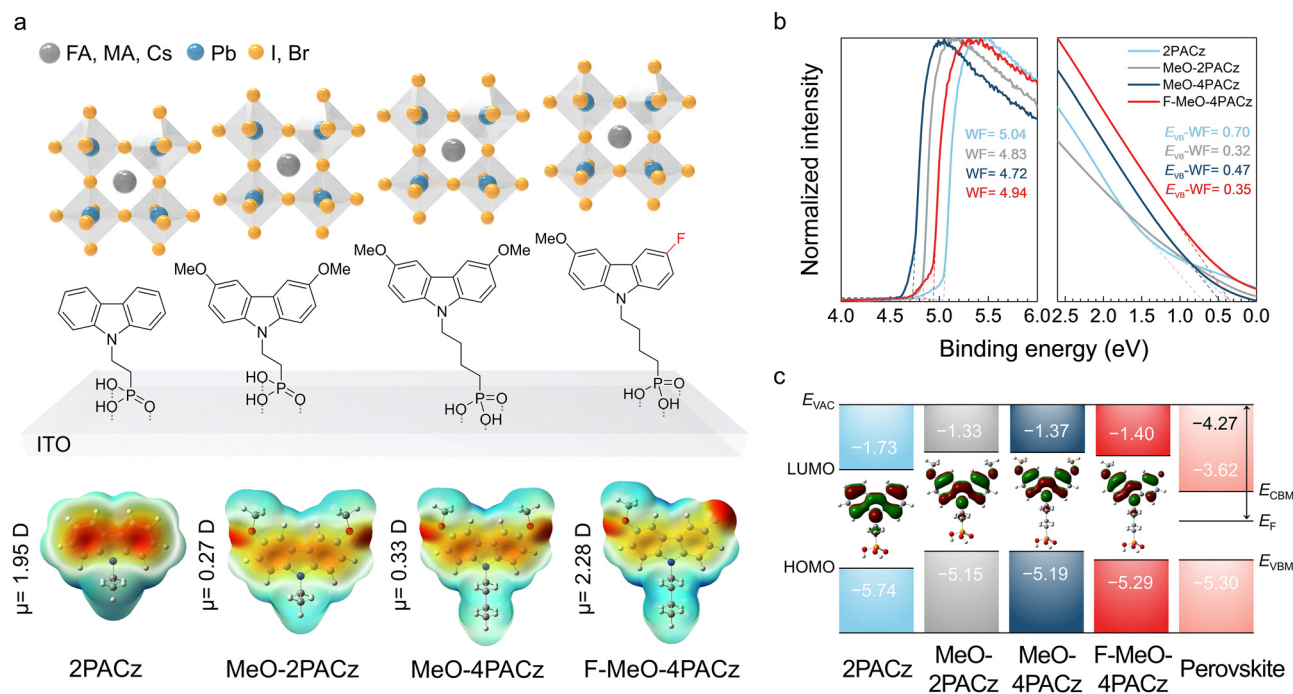


**Fig. 1** Chemical structure and electrical property of the SAMs. (a) Schematic representation of the SAMs structures, dipole moments, and electrostatic potential distributions. (b) UPS spectra showing the secondary electron cut-off region and the valence band onset. (c) Energy level alignment and electron density distribution of perovskite in conjunction with various hole-selective layers.

including the MeO-4PACz and F-MeO-4PACz molecules that we synthesized. Phosphonic acid anchor groups are adsorbed on the indium-doped tin oxide (ITO) layer, modulating the WF through the dipole moment contribution of SAM molecules and thus facilitating charge extraction.<sup>2,35</sup> The detailed synthesis methods and <sup>1</sup>H NMR spectra are provided in the experimental section and Fig. S21–S29 (SI). The methoxy substitution

on the carbazole core is known to passivate interfacial defects in perovskite solar cells.<sup>2,31,32</sup> However, the bilaterally substituted methoxy group pair increases the symmetry of the SAM molecules, causing the molecular dipole moments, calculated using density functional theory (DFT), to be significantly reduced from 1.95 D (for 2PACz) to 0.27 D and 0.33 D for MeO-2PACz and MeO-4PACz, respectively. The reduced

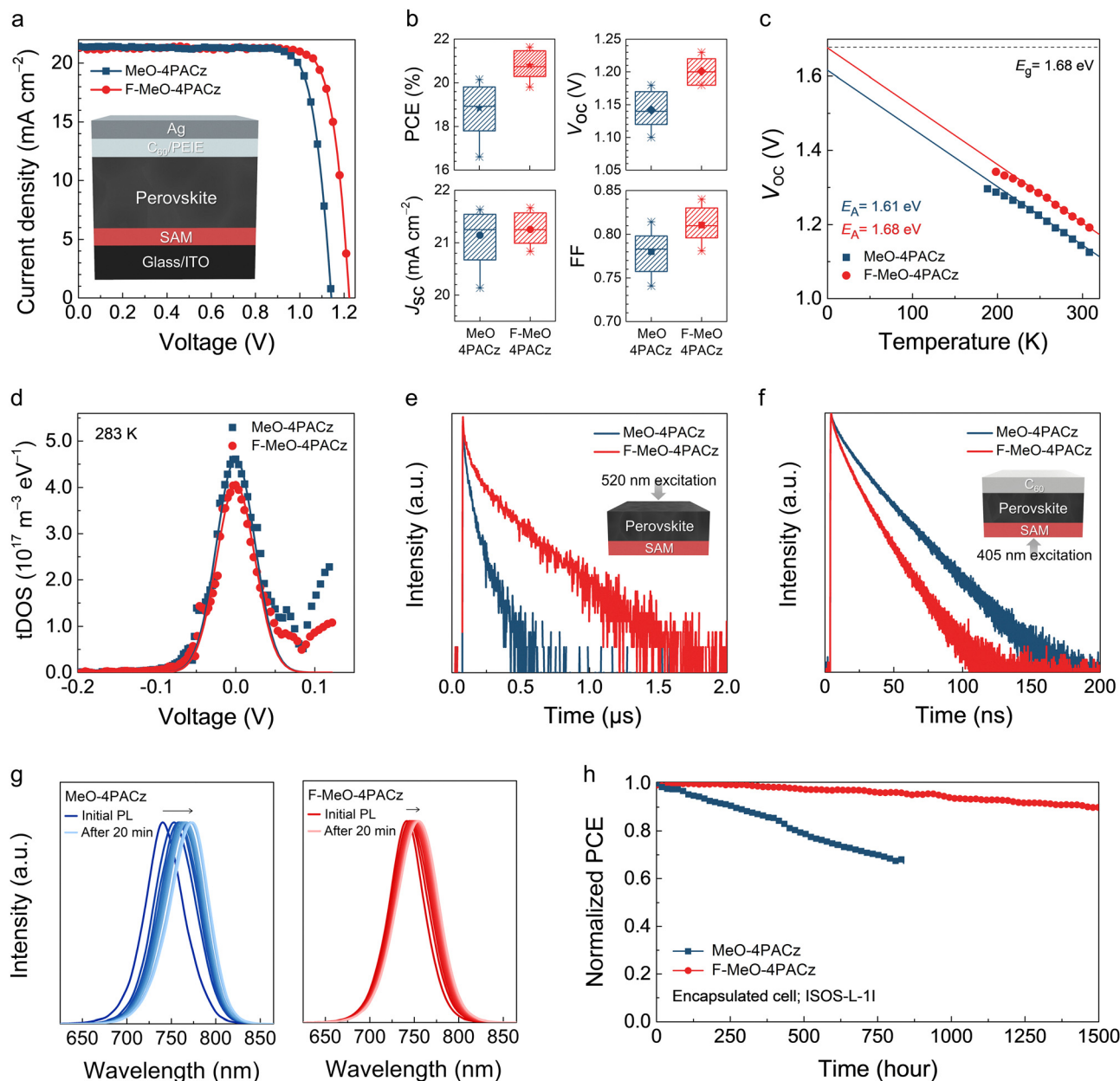


Fig. 2 Single-junction device performance, charge dynamics, and stability. (a) Representative  $J$ - $V$  curves of the perovskite single-junction solar cells with different SAMs. (b) Statistical  $J$ - $V$  parameters with varying substituent of the SAMs. These statistics, derived from measurements of over 80 active areas, present the minimum, mean, and maximum values as symbols, with the box representing the 10th and 90th percentiles. (c) Temperature dependence of  $V_{oc}$  and recombination activation energy ( $E_A$ ) determined by 0 K intercept from linear extrapolation of the perovskite single-junction solar cells. (d) tDOS plots of the inflection frequencies determined from the derivative  $-fdC/df$ . (e) and (f) Time-resolved PL spectra of the perovskite absorbers. The inset of (e) shows the results obtained by exciting the front side of the ITO/SAM/perovskite film using a 520 nm laser with a penetration depth of 217 nm. The inset of (f) shows the spectra obtained by exciting the back side of the ITO/SAM/perovskite/C<sub>60</sub> film with a 405 nm laser, exhibiting a penetration depth of 27 nm. (g) PL analysis of the perovskite absorbers under continuous laser irradiation for 20 min. (h) Long-term stability of the perovskite single-junction devices under 1-sun illumination with encapsulation (ISOS-L-11).

molecular dipole moment diminishes the WF shift, impeding favourable energy alignment between perovskites and SAMs.<sup>25</sup> On the other hand, the substitution of one methoxy group with a fluorine functional group (F-MeO-4PACz) gives rise to an asymmetric molecular structure, resulting in an imbalanced charge distribution due to the electron-withdrawing effect. As a result, the molecular dipole moment increases to 2.28 D, while preserving the defect passivation effect of the methoxy group, which is expected to facilitate charge extraction.

The effect of fluorine substitution on the energy levels has been experimentally investigated using ultraviolet photoelectron spectroscopy (UPS) of the SAMs on ITO/glass substrates (Fig. 1b). The UPS spectra in the secondary electron cut-off and valence band onset regions show that 2PACz and F-MeO-4PACz, which have larger dipole moments, exhibit higher WFs compared to those with smaller dipole moments, such as MeO-2PACz and MeO-4PACz. A direct comparison between MeO-4PACz and F-MeO-4PACz shows that fluorine substitution increases the WF from 4.72 eV to 4.94 eV. The contact potential difference (CPD) measured by Kelvin probe force microscopy (KPFM) also shows more negative value, meaning a larger WF, for F-MeO-4PACz compared with MeO-4PACz (Fig. S1, SI). Fig. 1c presents the energy band levels of SAMs and perovskite obtained by UPS, which is in a good agreement with those calculated by DFT (Fig. S2, SI). The HOMO level of 2PACz (−5.74 eV) shifts upward upon methoxy substitution (−5.15 eV for MeO-2PACz) because the methoxy group, as an electron-donating substituent, increases the electron density in the  $\pi$ -conjugation system as can be confirmed from the electron density distribution in Fig. 1c. On the other hand, the fluorine group functions as an electron-withdrawing substituent, reducing the electron density by creating electron holes. Thus, the HOMO level of MeO-4PACz shifts downward from −5.19 eV to −5.29 eV upon substitution of methoxy group with fluorine (F-MeO-4PACz), which is close to the HOMO level of the perovskite absorber material. Consequently, the F-MeO-4PACz molecule is believed to be the best choice for the SAM of the perovskite solar cell, as it exhibits a large WF while preserving the defect passivation effect of the methoxy group and providing appropriate band alignment with the perovskite layer.

### Single-junction performances

Fig. 2a compares the current density–voltage ( $J$ – $V$ ) curves of opaque single-junction wide-bandgap perovskite solar cells as a function of fluorine substitution, with the inset illustrating the schematic structure of the device, and their photovoltaic properties and diode parameters obtained from dark  $J$ – $V$  curves are summarized in Table S1 (SI). The bandgap energy ( $E_g$ ) of the perovskite absorber layer with the composition  $\text{Cs}_{0.05}(\text{FA}_{0.77}\text{MA}_{0.23})_{0.95}\text{Pb}(\text{I}_{0.77}\text{Br}_{0.23})_3$  is 1.68 eV (Fig. S3, SI), which is an optimal value for a double-junction Si tandem. To evaluate the specific impact of the fluorine substituent, two SAM molecules, MeO-4PACz and F-MeO-4PACz, have been selected for further investigation. The optimal concentration of the SAM coating solution was determined to be 1 mM based on our preliminary experiments (Fig. S4, SI), in which the cell

performance was predominantly influenced by the fill factor (FF). Notably, higher concentrations resulted in a reduced FF, suggesting that an increased SAM thickness contributes to higher series resistance. The  $J$ – $V$  curves demonstrate that the fluorine substitution increases the open-circuit voltage ( $V_{\text{OC}}$ ) and FF, while the short-circuit current density ( $J_{\text{SC}}$ ) remains essentially unchanged. The reduction in shunt conductance ( $G_{\text{sh}}$ ), reverse saturation current density ( $J_0$ ), and series resistance ( $R_s$ ), as shown in Table S1 (SI), is consistent with the observed increase in  $V_{\text{OC}}$  and FF. The statistical  $J$ – $V$  parameters, presented in Fig. 2b, also exhibit similar trends. Consequently, the F-MeO-4PACz-based device achieves a high PCE of 21.62% with  $J_{\text{SC}}$ ,  $V_{\text{OC}}$ , and FF values of 21.23 mA cm<sup>−2</sup>, 1.22 V, and 0.83, respectively. No  $J$ – $V$  hysteresis effect is observed, and the  $J_{\text{SC}}$  value obtained from the  $J$ – $V$  curve closely matches the value calculated from the external quantum efficiency (EQE) curve (Fig. S5, SI). The grain sizes, absorbance, and crystallinity of the perovskite layer were barely affected by the type of SAM molecules (Fig. S6, SI), resulting in similar  $J_{\text{SC}}$  values for the two samples. On the other hand, the activation energy ( $E_A$ ) of the main recombination process<sup>5</sup> obtained from the  $y$ -intercept of the fitted line in the temperature dependency of  $V_{\text{OC}}$  (Fig. 2c), increases from 1.61 eV to 1.68 eV with the fluorine-modified SAM molecules. The transient photovoltage decay (TPVD) measurement also reveals that the F-MeO-4PACz device exhibits a longer carrier lifetime (Fig. S7, SI), confirming that the interfacial electrical traps were effectively passivated by the fluorine substitution in the SAM molecule. The lower trap density of states (tDOS, Fig. 2d), higher defect activation energy obtained from thermal admittance spectroscopy (TAS, Fig. S8, SI), and the smaller trap-filling limit voltage ( $V_{\text{TFL}}$ ) derived from space charge limited current (SCLC) analysis of the hole-only device (Fig. S9, SI) further support the reduction of defects and trap states at the perovskite/HTL interface. In addition to the lower HOMO level of the F-MeO-4PACz molecule and the band-shift effect induced by its larger dipole moment, the interfacial defect passivation effect likely contributes to the increased  $V_{\text{OC}}$  of the fluorine-substituted device. The effect of the fluorine substituent in the SAM on the hole extraction at the perovskite/HTL interface was investigated using steady-state (SS) and time-resolved (TR) photoluminescence (PL) measurements. Fig. 2e and f compare the TR-PL curves of the perovskite layer deposited on the SAM depending on the fluorine substitution, with the insets schematically illustrating the measurement conditions. The F-MeO-4PACz sample exhibits slower decay with 520 nm probing light incident from the perovskite side, indicating reduced charge recombination, which is consistent with the stronger intensity observed in the SS-PL measurement (Fig. S10, SI). In order to minimize the influence of the charge recombination on the PL results, a  $\text{C}_{60}$  ETL was additionally deposited on top of the perovskite layer, and probing light with a shorter wavelength of 405 nm was illuminated from the SAM side. By using the probing light with a higher absorption coefficient incident from the contact side, photoexcited charge carriers can be preferentially generated near the interface, while photoelectrons generated outside the interface can be

effectively extracted by the  $C_{60}$  layer.<sup>36</sup> Under the modified measurement conditions, the F-MeO-4PACz sample exhibits faster decay and stronger PL quenching (Fig. S11, SI), indicating that fluorine substitution in the SAM molecule actually enhances hole extraction from the perovskite layer. The enhanced interfacial charge extraction also contributes to the reduced  $R_s$  of the device, and consequently, to the higher FF.

The fluorine substitution also influenced the photostability of the wide-bandgap perovskite thin films consisting of mixed halides, as can be seen from the peak shift in the PL spectra under continuous laser illumination (Fig. 2g). Both samples show a gradual red shift of the luminescence peaks during laser illumination, which is a characteristic indicator of halide segregation in mixed-halide perovskites.<sup>37,38</sup> However, the peak shift in the F-MeO-4PACz thin film is slower than the unmodified counterpart, suggesting that fluorine substitution effectively suppresses halide segregation, thereby enhancing

photostability. Although the mechanism by which the fluorine-modified SAM molecules retard the halide segregation process remains unclear, it can be hypothesized that the fluorine functional group impedes the migration of halide vacancies. Consequently, the atomic diffusion of halogen atoms, which drives halide segregation, may be suppressed. The long-term operational stability of the encapsulated semi-transparent perovskite solar cells was characterized by the maximum power point tracking (MPPT) measurement following the ISOS-L-1I protocol, using a white LED light source (Fig. 2h). The F-MeO-4PACz-based device maintains 90% of its initial efficiency up to 1500 h, while the unsubstituted counterpart exhibits a 30% decrease in efficiency after 750 h, demonstrating a significant improvement in long-term operational stability due to the fluorine substitution in the SAM molecule (Fig. S12, SI). In addition, the single-junction transparent device with F-MeO-4PACz exhibited enhanced thermal

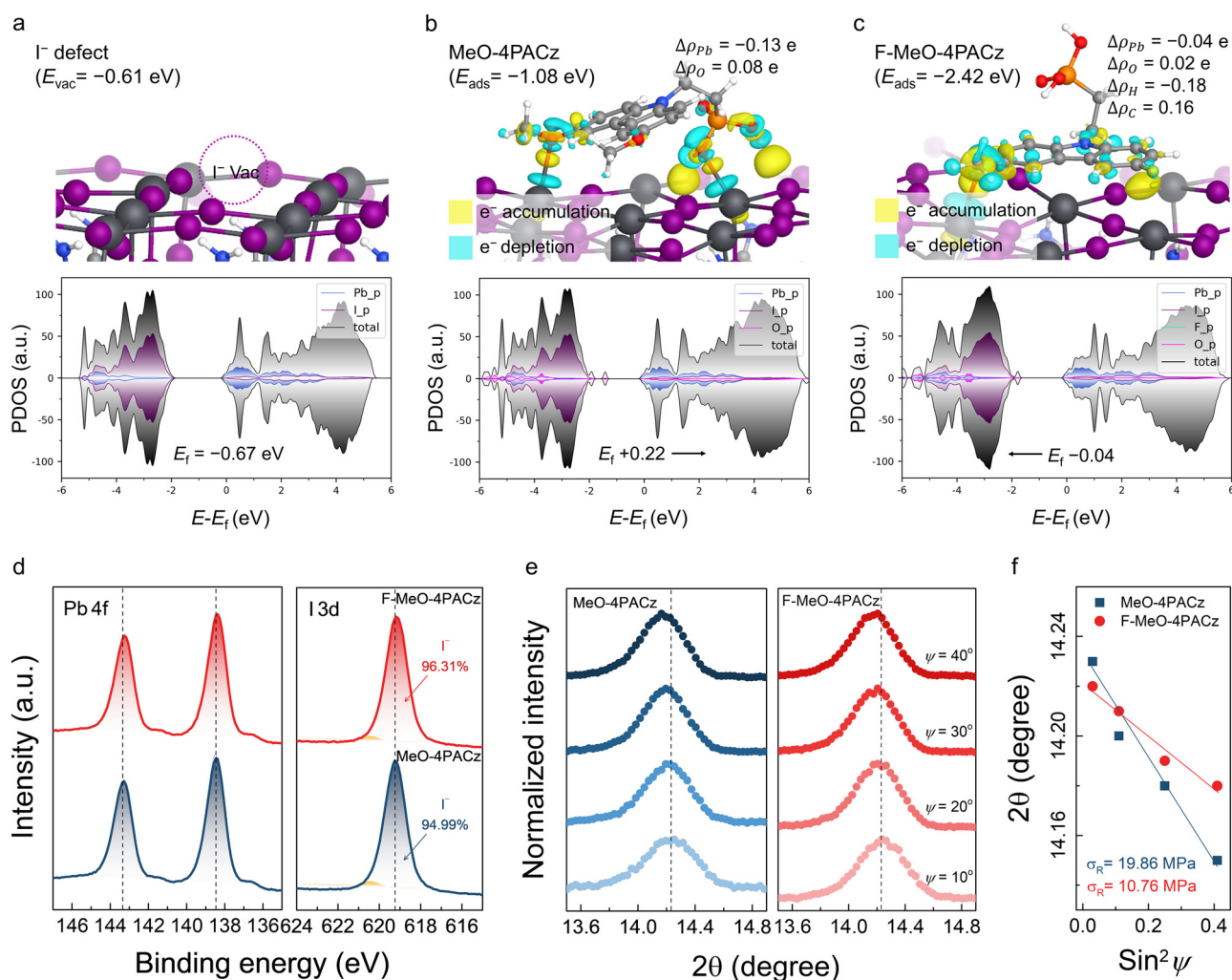


**Fig. 3** Buried interface properties. (a)–(c) Computational simulations of the SAM/perovskite adsorption model. Thermodynamically stable iodide anti-site defect model and the defect formation energy (a). The preferred adsorption model, adsorption energy, Bader charge distribution, and energy level state of the MeO-4PACz (b) and F-MeO-4PACz (c) with perovskites in the presence of iodide anti-site defect. (d) XPS spectra of the Pb 4f and I 3d, (e) GIXRD pattern, and (f) the comparison of residual stress of the perovskite bottom surface that were peeled off from the MeO-4PACz or F-MeO-4PACz/perovskite interface.

and light stability compared to the unsubstituted SAM, maintaining 92% of its initial efficiency under continuous illumination for 100 h (Fig. S13, SI). The enhanced stability can be attributed to the suppression of halide segregation and the prevention of charge accumulation at the perovskite/HTL interface, resulting from the facilitated charge extraction.

### Buried interface properties

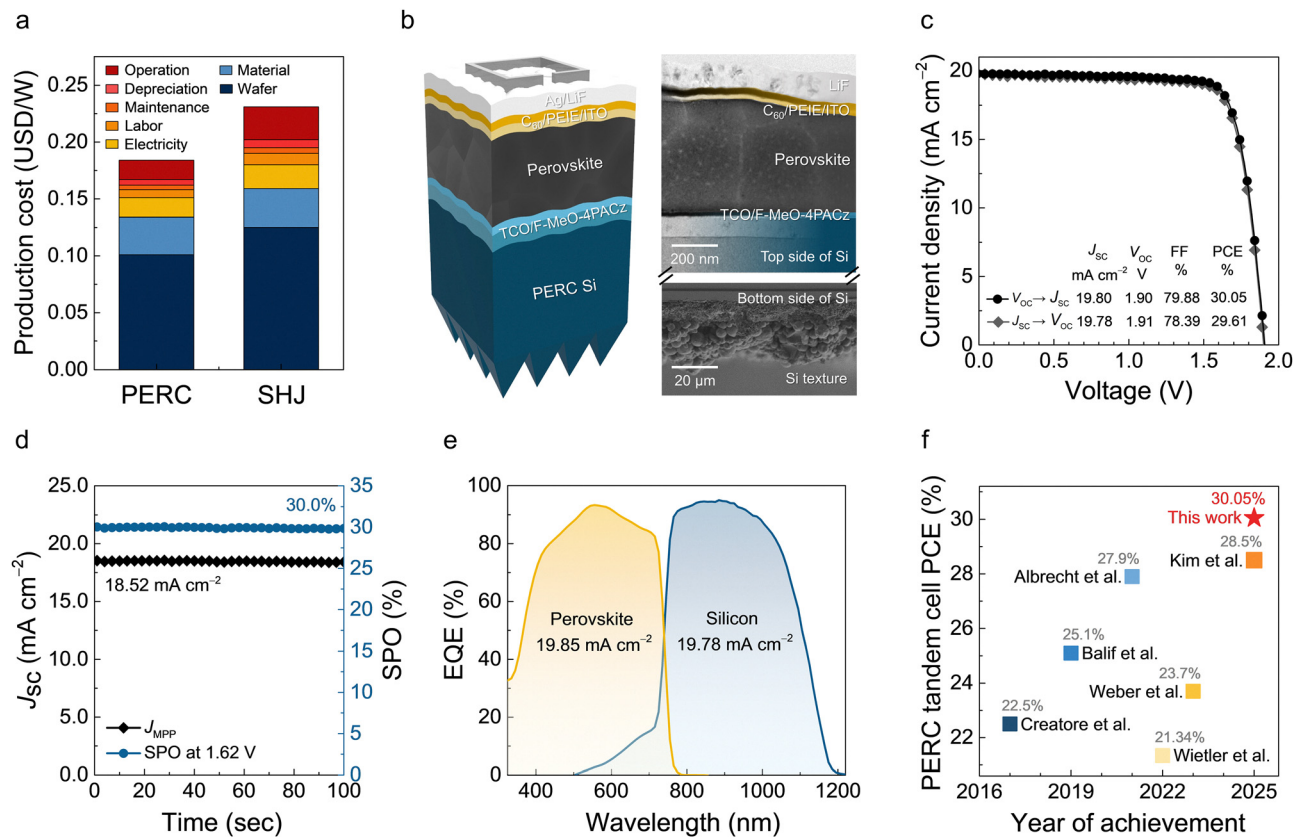
The properties of the buried interface were further investigated using DFT calculations. The binding energy and electron density calculations reveal that the formation energy of the  $I^-$  vacancy is  $-0.61$  eV, indicating that the  $I^-$  vacancy within the perovskite lattice is thermodynamically stable (Fig. 3a). Thus, further calculations were conducted based on the presence of  $I^-$  vacancies in the perovskite lattice. The adsorption energies for different possible adsorption modes of the SAM molecules were calculated in the presence of the  $I^-$  vacancies in the perovskite lattice (Fig. S14, SI), and Fig. 3b and c show the most energetically favourable adsorption modes of SAM molecules with and without fluorine substitution. In the case of MeO-4PACz, both the methoxy and phosphonic acid groups tend to align toward the perovskite surface, resulting in the lowest adsorption energy of  $-1.08$  eV. In contrast, for F-MeO-4PACz, the methoxy group is oriented toward the perovskite surface, while the phosphonic acid group points to the opposite direction. This orientation is favourable for efficient hole extraction at the ITO/SAM/perovskite interface. The electron density distribution and Bader charge analysis were also influenced by the fluorine substitution (Fig. S15, SI). For MeO-4PACz, the O atoms in methoxy groups of the SAM molecule form strong covalent bonds with the Pb atom in the perovskite lattice, resulting in Bader charges of  $-0.13 e$  for Pb and  $0.08 e$  for O. The negative and positive Bader charges indicate the loss and gain of electrons, respectively. In contrast, for F-MeO-4PACz, Pb loses  $0.04 e$  and O gains  $0.02 e$ , as it has only one O atom from the methoxy group near the perovskite surface, whereas MeO-4PACz has five O atoms (two in the methoxy groups and three in the phosphonic acid group). Notably, C atoms of the perovskite gain  $0.16 e$  and H atoms in the methoxy group lose  $0.18 e$  only for F-MeO-4PACz, due to the high electronegativity of F, exhibiting dipole-dipole interactions at the SAM/perovskite interface. As a result, the Fermi energy of the perovskite shifts by  $-0.04$  eV for F-MeO-4PACz and  $+0.22$  eV for MeO-4PACz. Consequently, the energy band alignment is adjusted toward more favourable energy levels, facilitating charge transfer between SAM and perovskite, which is consistent with the faster charge extraction results in Fig. 1. It should also be noted that the total adsorption energy of  $-2.42$  eV for F-MeO-4PACz is more negative than that of MeO-4PACz, indicating that F-MeO-4PACz forms a more energetically favourable adsorption and contributes to stabilizing the perovskite lattice with the  $I^-$  vacancies.

Fig. 3d shows X-ray photoelectron spectroscopy (XPS) spectra of the bottom surface of perovskite layers that were peeled off from the SAM/perovskite layers. No residual SAM molecules were detected, as confirmed by the XPS spectrum, which

showed no trace of fluorine (Fig. S16, SI). The perovskite layer deposited on the fluorine-substituted SAM exhibits a slight peak shift of the Pb 4f peak toward lower binding energy compared with the unsubstituted counterpart. This observation is consistent with DFT calculations and Bader charge analysis, which indicate less oxidation of the Pb atoms with fluorine substitution.<sup>39,40</sup> I 3d spectrum also exhibits a slightly higher  $I^-$  content for F-MeO-4PACz, indicating the fluorine substitution presumably suppresses the formation of  $I^-$  vacancies at the interface.<sup>41</sup> Fig. 3e presents grazing incident X-ray diffraction (GIXRD) patterns of the (110) plane of the perovskite buried interface, with and without fluorine substitution, obtained from the detached surfaces. The (110) peak shifts to higher angles with increasing incident angle ( $\psi$ ), and this dependence can be used to evaluate the residual stress ( $\sigma_R$ ) of the thin films as shown in Fig. 3f.<sup>42,43</sup> The calculated  $\sigma_R$  was significantly reduced from 19.86 MPa to 10.76 MPa for F-MeO-4PACz, indicating that the fluorine substitution can alleviate the lattice distortion of perovskite films, particularly near the perovskite/SAM interface. This result is also qualitatively consistent with the DFT calculations, which show that F-MeO-4PACz stabilizes the perovskite lattice with the  $I^-$  vacancies.

### PERC-tandem performances

Most high-efficiency perovskite tandem cells have been demonstrated using silicon heterojunction (SHJ) bottom cells, owing to their superior performance compared to other types of Si cells. However, the PERC cell still holds advantages over SHJ cells as the most widely used and cost-effective commercial silicon solar cell.<sup>44</sup> Fig. 4a shows that the power production cost of the SHJ cell is approximately 27% higher than that of the PERC cell, which should contribute to the improved cost-effectiveness of the final tandem cells. In the same context, the highly efficient and stable wide-bandgap perovskite top cells, featuring F-MeO-4PACz SAM, have been integrated with the PERC bottom cell, as shown in Fig. 4b. Fig. 4c shows the  $J-V$  curve of the best-performing 2T perovskite/Si tandem cell, consisting of the F-MeO-4PACz-based perovskite top cell and a PERC bottom cell. The measured parameters for this tandem cell are a  $J_{SC}$  value of  $19.80 \text{ mA cm}^{-2}$ , a  $V_{OC}$  value of 1.90 V, a FF value of 79.88%, and a conversion efficiency of 30.05% with an aperture size of  $1 \text{ cm}^2$ . Both MeO- and F-MeO-4PACz SAMs worked effectively on the SHJ bottom cell (Fig. S17, SI). No hysteresis effect is observed in the  $J-V$  curve, and the steady-state power output (SPO) measurement demonstrates a stabilized efficiency of 30.0% (Fig. 4d), which is consistent with the value obtained from the  $J-V$  measurement. After 1000 min, the tandem cell retained  $>98\%$  of its initial efficiency, indicating stable device performance (Fig. S18, SI). The solar cell parameters of the individual subcells (*i.e.*, a transparent wide-bandgap perovskite single-junction solar cell and a PERC bottom cell, obtained by removing the top cell from the tandem cell) can be found from their respective  $J-V$  curves (Fig. S19 and S20, SI). Notably, the  $V_{OC}$  of the tandem cell (1.90 V) is close to the sum of the subcell  $V_{OC}$  values (0.67 V for the bottom cell and 1.21 V for the top cell), and the tandem  $J_{SC}$  closely matches the



**Fig. 4** 2T tandem device performance and stability. (a) Comparison of power production costs in PERC (20.5% PCE) and SHJ (22.5% PCE) cells. The cost analysis assumes 1 GW of annual production facilities in China, as reported by NREL. The figures are modified versions of the original figure in ref. 44. (b) Schematic stack and cross-section TEM and FE-SEM images of an our 2T perovskite/Si tandem device. (c) and (d)  $J$ - $V$  curves (c), SPO near maximum power point without encapsulation (d), subcell EQE spectra (e), and the efficiency trend of PERC-based tandem device (f) of the champion 2T perovskite/Si tandem device.

value calculated from the subcell EQE curves (Fig. 4e). The champion efficiency of over 30% achieved in this study represents the highest reported performance for 2T perovskite/Si solar cells employing a PERC bottom cell (Fig. 4f).<sup>45–50</sup>

30.05% was achieved for a cost-effective monolithic 2T perovskite/Si tandem solar cell, which is the highest efficiency reported for those utilizing the commercial PERC bottom cell.

## Conclusions

We investigated the effects of asymmetric fluorine substitution in carbazole-based SAM molecules (F-MeO-4PACz) on the performance of wide-bandgap perovskite solar cells and their monolithic Si tandem cells. F-MeO-4PACz exhibited a larger dipole moment, higher WF, and a deeper HOMO level compared to the unsubstituted counterpart (MeO-4PACz), leading to an increased  $V_{oc}$ . Additionally, it facilitated more efficient charge transfer at the interfaces due to the improved energy band alignment with perovskite films, resulting in an increased FF. DFT calculations confirmed that the modification enhances the alignment of the SAM molecules and stabilizes the perovskite/SAM interface, contributing to improved  $V_{oc}$  and long-term operational stability of the perovskite solar cells. The best wide-bandgap single-junction top cell exhibited a high certified efficiency of 20.14% and a decent operational stability of 1500 hours ( $T_{90}$ ). Finally, a high conversion efficiency of

## Author contributions

MSK, IJP and JYK conceived the project. SJP, IJP and JYK designed the experiments and characterization. CY and MSK optimized and characterized the functional groups of SAM molecules. CY and SS conducted NMR analysis and DFT calculations of SAM molecules. KIS and JWH carried out calculations for the SAM-perovskite adsorption model. SJP conducted fabrication and characterization of wide-bandgap perovskite films and devices. SJP, SKH and JHP executed defect analysis and EQE measurement of the single and double junction devices. SJP conducted fabrication and characterization of 2T perovskite/Si tandem cells. YJC, SJP and GPH conducted long-term stability measurements of wide-bandgap perovskite devices. SJP, CY, MSG, IJP and JYK discussed the results. SJP, CY, KIS, MSK, IJP and JYK wrote the manuscript. All authors examined the manuscript and provided feedback for revisions.

## Conflicts of interest

The authors declare no competing interests.

## Data availability

The data supporting this article have been included as part of the SI. See DOI: <https://doi.org/10.1039/d5ee02650d>

## Acknowledgements

The authors acknowledge Hanwha Qcells Co. Ltd. for supplying Si bottom cells for tandem cell fabrication. This work was supported by the National Research Foundation of Korea (NRF) grant funded by the Korea Government (MSIT) (RS-2021-NR057352, RS-2023-00273532, and RS-2024-00418209) and the Korea Institute of Energy Technology Evaluation and Planning (KETEP), the Ministry of Trade, Industry and Energy (MOTIE) of the Republic of Korea (RS-2023-00302107).

## Notes and references

- D. H. Kim, C. P. Muzzillo, J. Tong, A. F. Palmstrom, B. W. Larson, C. Choi, S. P. Harvey, S. Glynn, J. B. Whitaker, F. Zhang, Z. Li, H. Lu, M. F. A. M. van Hest, J. J. Berry, L. M. Mansfield, Y. Huang, Y. Yan and K. Zhu, *Joule*, 2019, 3, 1734–1745.
- A. Al-Ashouri, A. Magomedov, M. Roß, M. Jošt, M. Talaikis, G. Chistiakova, T. Bertram, J. A. Márquez, E. Köhnen, E. Kasparavičius, S. Levenco, L. Gil-Escrig, C. J. Hages, R. Schlatmann, B. Rech, T. Malinauskas, T. Unold, C. A. Kaufmann, L. Korte, G. Niaura, V. Getautis and S. Albrecht, *Energy Environ. Sci.*, 2019, 12, 3356–3369.
- D. Kim, H. J. Jung, I. J. Park, B. W. Larson, S. P. Dunfield, C. Xiao, J. Kim, J. Tong, P. Boonmongkolras, S. G. Ji, F. Zhang, S. R. Pae, M. Kim, S. B. Kang, V. Dravid, J. J. Berry, J. Y. Kim, K. Zhu, D. H. Kim and B. Shin, *Science*, 2020, 368, 155–160.
- S. G. Ji, I. J. Park, H. Chang, J. H. Park, G. P. Hong, B. K. Choi, J. H. Jang, Y. J. Choi, H. W. Lim, Y. J. Ahn, S. J. Park, K. T. Nam, T. Hyeon, J. Park, D. H. Kim and J. Y. Kim, *Joule*, 2022, 6, 2390–2405.
- S. K. Hwang, S. J. Park, J. H. Park, J. H. Yoon, J. Yu Cho, D. K. Cho, J. Heo, G. Y. Kim and J. Y. Kim, *Small*, 2024, 20, 2307175.
- R. Lin, J. Xu, M. Wei, Y. Wang, Z. Qin, Z. Liu, J. Wu, K. Xiao, B. Chen, S. M. Park, G. Chen, H. R. Atapattu, K. R. Graham, J. Xu, J. Zhu, L. Li, C. Zhang, E. H. Sargent and H. Tan, *Nature*, 2022, 603, 73–78.
- Y. J. Choi, S. Y. Lim, J. H. Park, S. G. Ji and J. Y. Kim, *ACS Energy Lett.*, 2023, 8, 3141–3146.
- S. Liu, Y. Lu, C. Yu, J. Li, R. Luo, R. Guo, H. Liang, X. Jia, X. Guo, Y.-D. Wang, Q. Zhou, X. Wang, S. Yang, M. Sui, P. Müller-Buschbaum and Y. Hou, *Nature*, 2024, 628, 306–312.
- R. Wang, T. Huang, J. Xue, J. Tong, K. Zhu and Y. Yang, *Nat. Photonics*, 2021, 15, 411–425.
- T. Leijtens, K. A. Bush, R. Prasanna and M. D. McGehee, *Nat. Energy*, 2018, 3, 828–838.
- F. Sahli, J. Werner, B. A. Kamino, M. Bräuninger, R. Monnard, B. Paviet-Salomon, L. Barraud, L. Ding, J. J. Diaz Leon, D. Sacchetto, G. Cattaneo, M. Despeisse, M. Boccard, S. Nicolay, Q. Jeangros, B. Niesen and C. Ballif, *Nat. Mater.*, 2018, 17, 820–826.
- P. Tockhorn, J. Sutter, A. Cruz, P. Wagner, K. Jäger, D. Yoo, F. Lang, M. Grischek, B. Li, J. Li, O. Shargaieva, E. Unger, A. Al-Ashouri, E. Köhnen, M. Stolterfoht, D. Neher, R. Schlatmann, B. Rech, B. Stannowski, S. Albrecht and C. Becker, *Nat. Nanotechnol.*, 2022, 17, 1214–1221.
- Y. Hou, E. Aydin, M. De Bastiani, C. Xiao, F. H. Isikgor, D.-J. Xue, B. Chen, H. Chen, B. Bahrami, A. H. Chowdhury, A. Johnston, S.-W. Baek, Z. Huang, M. Wei, Y. Dong, J. Troughton, R. Jalmoood, A. J. Mirabelli, T. G. Allen, E. Van Kerschaver, M. I. Saidaminov, D. Baran, Q. Qiao, K. Zhu, S. De Wolf and E. H. Sargent, *Science*, 2020, 367, 1135–1140.
- W. Yan, C. Li, C. Peng, S. Tan, J. Zhang, H. Jiang, F. Xin, F. Yue and Z. Zhou, *Adv. Mater.*, 2024, 36, 2312170.
- National Renewable Energy Laboratory, “Best Research-Cell Efficiency Chart”, 2025, <https://www.nrel.gov/pv/cell-efficiency.html>.
- D. P. McMeekin, G. Sadoughi, W. Rehman, G. E. Eperon, M. Saliba, M. T. Hörlantner, A. Haghighirad, N. Sakai, L. Korte, B. Rech, M. B. Johnston, L. M. Herz and H. J. Snaith, *Science*, 2016, 351, 151–155.
- H. Chen, C. Liu, J. Xu, A. Maxwell, W. Zhou, Y. Yang, Q. Zhou, A. S. R. Bati, H. Wan, Z. Wang, L. Zeng, J. Wang, P. Serles, Y. Liu, S. Teale, Y. Liu, M. I. Saidaminov, M. Li, N. Rolston, S. Hoogland, T. Filleter, M. G. Kanatzidis, B. Chen, Z. Ning and E. H. Sargent, *Science*, 2024, 384, 189–193.
- J. Feng, Y. Jiao, H. Wang, X. Zhu, Y. Sun, M. Du, Y. Cao, D. Yang and S. Liu, *Energy Environ. Sci.*, 2021, 14, 3035–3043.
- J. Li, H. Wang, X. Y. Chin, H. A. Dewi, K. Vergeer, T. W. Goh, J. W. M. Lim, J. H. Lew, K. P. Loh, C. Soci, T. C. Sum, H. J. Bolink, N. Mathews, S. Mhaisalkar and A. Bruno, *Joule*, 2020, 4, 1035–1053.
- Z. Yang, W. Zhang, S. Wu, H. Zhu, Z. Liu, Z. Liu, Z. Jiang, R. Chen, J. Zhou, Q. Lu, Z. Xiao, L. Shi, H. Chen, L. K. Ono, S. Zhang, Y. Zhang, Y. Qi, L. Han and W. Chen, *Sci. Adv.*, 2021, 7, eabg3749.
- L. Tan, J. Zhou, X. Zhao, S. Wang, M. Li, C. Jiang, H. Li, Y. Zhang, Y. Ye, W. Tress, L. Ding, M. Grätzel and C. Yi, *Adv. Mater.*, 2023, 35, 2205027.
- Z. Li, Y. Zhao, X. Wang, Y. Sun, Z. Zhao, Y. Li, H. Zhou and Q. Chen, *Joule*, 2018, 2, 1559–1572.
- D. Yan, A. Cuevas, J. I. Michel, C. Zhang, Y. Wan, X. Zhang and J. Bullock, *Joule*, 2021, 5, 811–828.
- F. Fu, J. Li, T. C.-J. Yang, H. Liang, A. Faes, Q. Jeangros, C. Ballif and Y. Hou, *Adv. Mater.*, 2022, 34, 2106540.
- A. Al-Ashouri, E. Köhnen, B. Li, A. Magomedov, H. Hempel, P. Caprioglio, J. A. Márquez, A. B. Morales Vilches,

- E. Kasparavicius, J. A. Smith, N. Phung, D. Menzel, M. Grischek, L. Kegelman, D. Skroblin, C. Gollwitzer, T. Malinauskas, M. Jošt, G. Matič, B. Rech, R. Schlatmann, M. Topič, L. Korte, A. Abate, B. Stannowski, D. Neher, M. Stolterfoht, T. Unold, V. Getautis and S. Albrecht, *Science*, 2020, **370**, 1300–1309.
- 26 X. Y. Chin, D. Turkay, J. A. Steele, S. Tabean, S. Eswara, M. Mensi, P. Fiala, C. M. Wolff, A. Paracchino, K. Artuk, D. Jacobs, Q. Guesnay, F. Sahli, G. Andreatta, M. Boccard, Q. Jeangros and C. Ballif, *Science*, 2023, **381**, 59–63.
- 27 Z. Li, X. Sun, X. Zheng, B. Li, D. Gao, S. Zhang, X. Wu, S. Li, J. Gong, J. M. Luther, Z. A. Li and Z. Zhu, *Science*, 2023, **382**, 284–289.
- 28 G. Wang, J. Zheng, W. Duan, J. Yang, M. A. Mahmud, Q. Lian, S. Tang, C. Liao, J. Bing, J. Yi, T. L. Leung, X. Cui, H. Chen, F. Jiang, Y. Huang, A. Lambertz, M. Jankovec, M. Topič, S. Bremner, Y.-Z. Zhang, C. Cheng, K. Ding and A. Ho-Baillie, *Joule*, 2023, **7**, 2583–2594.
- 29 S. Mariotti, E. Köhnen, F. Scheler, K. Sveinbjörnsson, L. Zimmermann, M. Piot, F. Yang, B. Li, J. Warby, A. Musiienko, D. Menzel, F. Lang, S. Kessler, I. Levine, D. Mantione, A. Al-Ashouri, M. S. Härtel, K. Xu, A. Cruz, J. Kurpiers, P. Wagner, H. Köbler, J. Li, A. Magomedov, D. Mecerreyes, E. Unger, A. Abate, M. Stolterfoht, B. Stannowski, R. Schlatmann, L. Korte and S. Albrecht, *Science*, 2023, **381**, 63–69.
- 30 J. Liu, Y. He, L. Ding, H. Zhang, Q. Li, L. Jia, J. Yu, T. W. Lau, M. Li, Y. Qin, X. Gu, F. Zhang, Q. Li, Y. Yang, S. Zhao, X. Wu, J. Liu, T. Liu, Y. Gao, Y. Wang, X. Dong, H. Chen, P. Li, T. Zhou, M. Yang, X. Ru, F. Peng, S. Yin, M. Qu, D. Zhao, Z. Zhao, M. Li, P. Guo, H. Yan, C. Xiao, P. Xiao, J. Yin, X. Zhang, Z. Li, B. He and X. Xu, *Nature*, 2024, **635**, 596–603.
- 31 S. J. Park, S. Jeon, I. K. Lee, J. Zhang, H. Jeong, J.-Y. Park, J. Bang, T. K. Ahn, H.-W. Shin, B.-G. Kim and H. J. Park, *J. Mater. Chem. A*, 2017, **5**, 13220–13227.
- 32 C. Huang, W. Fu, C.-Z. Li, Z. Zhang, W. Qiu, M. Shi, P. Heremans, A. K. Y. Jen and H. Chen, *J. Am. Chem. Soc.*, 2016, **138**, 2528–2531.
- 33 L. Li, Y. Wang, X. Wang, R. Lin, X. Luo, Z. Liu, K. Zhou, S. Xiong, Q. Bao, G. Chen, Y. Tian, Y. Deng, K. Xiao, J. Wu, M. I. Saidaminov, H. Lin, C.-Q. Ma, Z. Zhao, Y. Wu, L. Zhang and H. Tan, *Nat. Energy*, 2022, **7**, 708–717.
- 34 W. Jiang, F. Li, M. Li, F. Qi, F. R. Lin and A. K. Y. Jen, *Angew. Chem., Int. Ed.*, 2022, **61**, e202213560.
- 35 T. J. Gardner, C. D. Frisbie and M. S. Wrighton, *J. Am. Chem. Soc.*, 1995, **117**, 6927–6933.
- 36 J. Wen, Y. Zhao, P. Wu, Y. Liu, X. Zheng, R. Lin, S. Wan, K. Li, H. Luo, Y. Tian, L. Li and H. Tan, *Nat. Commun.*, 2023, **14**, 7118.
- 37 M. C. Brennan, S. Draguta, P. V. Kamat and M. Kuno, *ACS Energy Lett.*, 2018, **3**, 204–213.
- 38 W. Rehman, D. P. McMeekin, J. B. Patel, R. L. Milot, M. B. Johnston, H. J. Snaith and L. M. Herz, *Energy Environ. Sci.*, 2017, **10**, 361–369.
- 39 R. Li, S. Zhang, H. Zhang, Z. Wang, X. Feng, Y. Du, T. Zhou, X. Chen, P. Liu, L. Liu, J. Zhang, Q. Chen, L. Xi, K. Zhao, S. Liu and Q. Tian, *Angew. Chem., Int. Ed.*, 2024, **63**, e202410600.
- 40 J. Chen, S.-G. Kim, X. Ren, H. S. Jung and N.-G. Park, *J. Mater. Chem. A*, 2019, **7**, 4977–4987.
- 41 H. Zhu, A. Liu, K. I. Shim, H. Jung, T. Zou, Y. Reo, H. Kim, J. W. Han, Y. Chen, H. Y. Chu, J. H. Lim, H.-J. Kim, S. Bai and Y.-Y. Noh, *Nat. Commun.*, 2022, **13**, 1741.
- 42 S. Liu, J. Li, W. Xiao, R. Chen, Z. Sun, Y. Zhang, X. Lei, S. Hu, M. Kober-Czerny, J. Wang, F. Ren, Q. Zhou, H. Raza, Y. Gao, Y. Ji, S. Li, H. Li, L. Qiu, W. Huang, Y. Zhao, B. Xu, Z. Liu, H. J. Snaith, N.-G. Park and W. Chen, *Nature*, 2024, **632**, 536–542.
- 43 H. Wang, C. Zhu, L. Liu, S. Ma, P. Liu, J. Wu, C. Shi, Q. Du, Y. Hao, S. Xiang, H. Chen, P. Chen, Y. Bai, H. Zhou, Y. Li and Q. Chen, *Adv. Mater.*, 2019, **31**, 1904408.
- 44 B. S. Michael Woodhouse, Ashwin Ramdas and Robert Margolis, *National Renewable Energy Laboratory*, 2019.
- 45 E. Köhnen, P. Wagner, F. Lang, A. Cruz, B. Li, M. Roß, M. Jošt, A. B. Morales-Vilches, M. Topič, M. Stolterfoht, D. Neher, L. Korte, B. Rech, R. Schlatmann, B. Stannowski and S. Albrecht, *Sol. RRL*, 2021, **5**, 2100244.
- 46 G. Nogay, F. Sahli, J. Werner, R. Monnard, M. Boccard, M. Despeisse, F. J. Haug, Q. Jeangros, A. Ingenito and C. Ballif, *ACS Energy Lett.*, 2019, **4**, 844–845.
- 47 N. Phung, D. Zhang, C. van Helvoirt, M. Verhage, M. Verheijen, V. Zardetto, F. Bens, C. H. L. Weijtens, L. J. Geerligs, W. M. M. Kessels, B. Macco and M. Creatore, *Sol. Energy Mater. Sol. Cells*, 2023, **261**, 112498.
- 48 Y. Wu, D. Yan, J. Peng, T. Duong, Y. Wan, S. P. Phang, H. Shen, N. Wu, C. Barugkin, X. Fu, S. Surve, D. Grant, D. Walter, T. P. White, K. R. Catchpole and K. J. Weber, *Energy Environ. Sci.*, 2017, **10**, 2472–2479.
- 49 S. Mariotti, K. Jäger, M. Diederich, M. S. Härtel, B. Li, K. Sveinbjörnsson, S. Kajari-Schröder, R. Peibst, S. Albrecht, L. Korte and T. Wietler, *Sol. RRL*, 2022, **6**, 2101066.
- 50 S. J. Park, G. P. Hong and J. Y. Kim, *ACS Energy Lett.*, 2025, **10**, 3743–3745.